AFRL-AFOSR-UK-TR-2022-0072

Supercritical Fuel Jets - Resolving Controversy

Linne, Mark
UNIVERSITY OF EDINBURGH (THE)
OLD COLLEGE, SOUTH BRIDGE
EDINBURGH, MIDLOTHIAN, EH8 9YL
GBR

07/01/2022
Final Technical Report

Air Force Research Laboratory
Air Force Office of Scientific Research
European Office of Aerospace Research and Development
Unit 4515 Box 14, APO AE 09421

REPORT DOCUMENTATION PAGE

PLEASE DO NOT RETURN YOUR FORM TO THE ABOVE ORGANIZATION.

1. REPORT DATE	2. REPORT TYPE	3. DATES COVERED	
20220701	Final	START DATE 20170115	END DATE 20220114

4. TITLE AND SUBTITLE
Supercritical Fuel Jets - Resolving Controversy

5a. CONTRACT NUMBER	5b. GRANT NUMBER	5c. PROGRAM ELEMENT NUMBER
	FA9550-17-1-0129	61102F
5d. PROJECT NUMBER	**5e. TASK NUMBER**	**5f. WORK UNIT NUMBER**

6. AUTHOR(S)
Mark Linne

7. PERFORMING ORGANIZATION NAME(S) AND ADDRESS(ES)
UNIVERSITY OF EDINBURGH (THE)
OLD COLLEGE, SOUTH BRIDGE
EDINBURGH, MIDLOTHIAN EH8 9YL
GBR

8. PERFORMING ORGANIZATION REPORT NUMBER

9. SPONSORING/MONITORING AGENCY NAME(S) AND ADDRESS(ES)	10. SPONSOR/MONITOR'S ACRONYM(S)	11. SPONSOR/MONITOR'S REPORT NUMBER(S)
EOARD UNIT 4515 APO AE 09421-4515	AFRL/AFOSR IOE	AFRL-AFOSR-UK-TR-2022-0072

12. DISTRIBUTION/AVAILABILITY STATEMENT
A Distribution Unlimited: PB Public Release

13. SUPPLEMENTARY NOTES

14. ABSTRACT
This report describes a four-year project (plus a one-year, no-cost extension) with the goal to generate quantitative data related to changes at the interface between a fuel jet and the surrounding gas; at high pressures and temperatures. This goal required the development of an experiment that provides an appropriate environment for investigation of fuel/gas interfaces. To generate more fundamental data using the new facilities also requires development and application of laser diagnostics. This project was co-funded; by AFOSR [total budget of $365,632, mostly for salaries and some travel] and by the UK Engineering and Physical Sciences Research Council [total budget of £354,166 (~ $492,000) mostly for equipment].

15. SUBJECT TERMS

16. SECURITY CLASSIFICATION OF:			17. LIMITATION OF ABSTRACT	18. NUMBER OF PAGES
a. REPORT U	b. ABSTRACT U	c. THIS PAGE U	SAR	15

19a. NAME OF RESPONSIBLE PERSON	19b. PHONE NUMBER *(Include area code)*
DOUGLAS SMITH	314 235 6013

Supercritical fuel jets - resolving controversy

AFOSR Grant FA9550-17-1-0129

Final Report

April, 2022

PI: Mark Linne
Professor of Combustion Engines
School of Engineering
University of Edinburgh

Summary

This report describes a four-year project (plus a one-year, no-cost extension) with the goal to generate quantitative data related to changes at the interface between a fuel jet and the surrounding gas; at high pressures and temperatures. This goal required the development of an experiment that provides an appropriate environment for investigation of fuel/gas interfaces. To generate more fundamental data using the new facilities also requires development and application of laser diagnostics.

This project was co-funded; by AFOSR [total budget of $365,632, mostly for salaries and some travel] and by the UK Engineering and Physical Sciences Research Council [total budget of £354,166 (~ $492,000) mostly for equipment].

Introduction

Modern transportation powerplants operate at very high pressures and temperatures, to achieve high efficiency, but those thermodynamic conditions are usually near or above the supercritical conditions for many pure hydrocarbon fuels. Based upon prior work[1], we hypothesized that when certain pure hydrocarbon fuels are injected into such conditions, the edges of the fuel jets transition from a well-defined interface (from which fuel evaporates) into a thickened mixing layer without a defined interface (through which fuel and air diffuse). The commonly assumed fuel spray structure would not exist in such a case. It is possible, however, that commercially available fuels do not undergo this transition, or just begin to do so, as mixtures of compounds have very different critical properties than do the pure substances.

We have chosen not to follow the more traditional and somewhat inconclusive path of imaging drops or sprays from commercial injectors. Instead, we have developed a laminar liquid jet that does not produce drops, because drops interfere with clear access to a well-defined interface that has a known initial condition and flow history. This jet will be more easily modelled as temperature-controlled pure liquids flow into a well-controlled cell filled

with nitrogen (we emphasize binary, inert mixtures to simplify modelling and to avoid the complications introduced by oxidation reactions).

The flow was imaged via shadowgraphy, but it was also investigated using laser diagnostics that allowed us to better characterize the evolving state. Harstad and Bellan[2] have argued that shadowgraphy is an inappropriate diagnostic for a transcritical interface because even if it has lost surface tension, the diffusive mixing region will be much thinner than the spatial resolution of an imaging system. The strong gradient in the index of refraction across that region could produce a shadowgram that looks like an intact interface. Even though we have used shadowgraphy to set up flows, we do not publish the results for this reason. Planar laser induced fluorescence normal to the jet axis has been used to characterize the chemical environment as a function of radial position away from the jet centerline. Changes in scattering of the input beam from the interface are also used to detect when the interface is breaking down. We have found that this flow is steady, uniform, and reproducible, so temperature distributions have been acquired using thermocouples.

Measurements were performed starting at the jet exit and progressing downstream until the column broke or disappeared, to characterize the evolution of the interface with time. For this work, the injected liquid was a fluoroketone.

Methods and Procedures

Chamber and ancillary equipment:

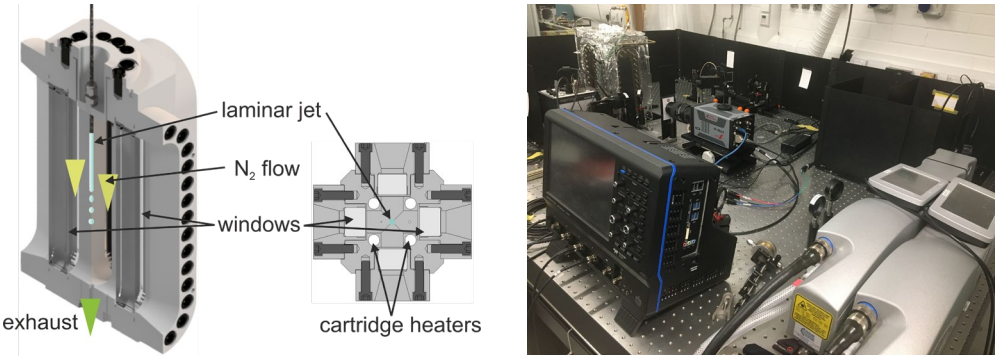

Figure 1. Chamber: a. side-view cut away, b. horizontal section, c. photograph of the entire experiment (the chamber is to the left, in the back).

The chamber that was developed for this project is depicted in Fig. 1. The chamber core is square in cross-section, with sides 73 x 73 *mm*, and it is 234 *mm* long. The interior is viewed through orthogonal window sets (the fused silica windows are 225 *mm* long, 32 *mm* wide and 20 *mm* thick). The injected liquid flows through a 0.8 *mm* inner diameter stainless steel tube that is 102 *mm* long (ensuring fully developed laminar flow) and it enters on centerline at the top. We do not observe any effects of velocity profile relaxation (which occurs after the flow has exited the nozzle); it makes no contribution to observations of the interface.

The liquid inside the nozzle is temperature controlled by ribbon heaters and a thermocouple at the entrance to the injection tube. The liquid control temperature has been calibrated by

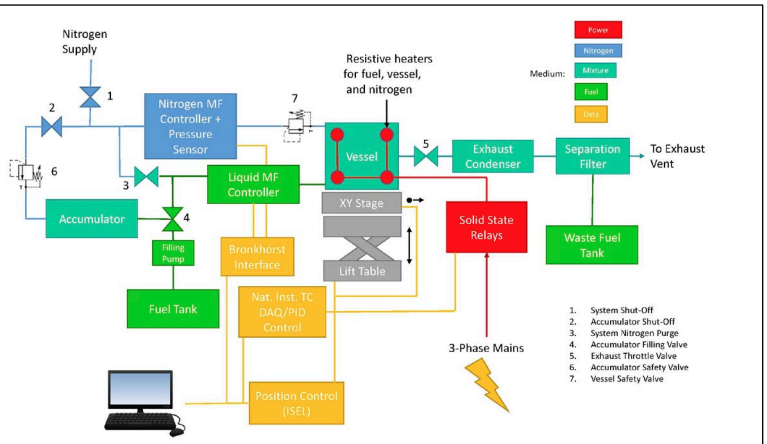

Figure 2. Chamber system schematic.

measurement of the fluid temperature at the tube exit (that thermocouple is removed when imaging the jet). Liquid temperatures reported here are therefore the temperatures at the tube exit. High pressure nitrogen is heated by four cartridge heaters that span the length of the chamber, but it reaches a peak temperature as it enters at the top. One cartridge heater contains a type K thermocouple which is used for chamber temperature control, although thermocouples measuring the gas temperature inside the chamber are used to set the control point. The nitrogen flows steadily and slowly through the heated chamber cavity to the exit at the bottom, together with injected liquid.

Temperature profiles taken inside the chamber using thermocouples (without a fluoroketone jet) indicate that the chamber gas temperature falls linearly with vertical distance, by 0.2 *K/cm*. The radial temperature profiles are flat to ± 1.1 *K*.

The mixture exiting the chamber passes through a choked flow valve, and the chamber pressure is controlled via the nitrogen flow rate using a mass flow controller (Bronkhorst IN-FLOW F-221MI, controlled by a Labview program, see Fig. 2). The liquid is delivered to the nozzle using a pressure accumulator and mass flow meter (Bronkhorst mini CORI-FLOW M14). The fluoroketone mass flow rate is set to 900 *gm/hr*, giving a nominal jet velocity of 0.31 *m/s*. The nitrogen flows slowly through the chamber to clear out vapor steadily, but it presents a quiescent gas to the liquid stream. We have confirmed that under steady conditions, fluoroketone vapors do not build up in the chamber because: 1) PLIF images of fluoroketone vapor do not indicate changes with time, and 2) the mass flow rate of nitrogen required to maintain the set chamber pressure remains constant.

To develop a high pressure and temperature chamber, starting from nothing, can consume 3 years easily; including design, approvals, build, test, analysis and modification, re-test, final approval etc. To develop a supercritical facility is doubly challenging, because many materials can go into solution with a supercritical fluid, including window seals. In an effort to avoid so much time-consuming equipment development, we imitated an existing design (with some support from the group that developed that design). Unfortunately, it was not possible to achieve a good pressure seal with that cell design, and so several years were consumed with required modifications and upgrades to the chamber. As a consequence, we were unable to perform as many flow experiments as originally planned.

The current chamber can reach over 350 ^{o}C gas temperature (set by the temperature limit on seals) and it can be pressurized to 90 bar. Unfortunately that temperature is not high enough for typical hydrocarbons (e.g. dodecane). We have therefore performed a

measurement campaign on fluoroketone [dodecafluoro-2-methylpentan-3-one ($CF_3CF_2C(O)CF(CF_3)_2$)], which has critical pressure and temperature that can be easily reached inside the chamber.

Fluoroketone:

The fluoroketone we have selected for study (Novec 649™ by 3M) is not a hydrocarbon and it is not a fuel (it is a refrigerant and fire retardant). It has useful properties as a surrogate, although the molecule is difficult to model with molecular dynamics. Novec has a low critical point, and it is relatively harmless. It is chemically stable, so it will not pyrolyze while under study, as some hydrocarbons do. This is an important point; if the pure injected liquid becomes a mixture of liquids via pyrolysis, its critical point can change significantly and uncontrollably. Novec also has a very high fluorescence yield so it does not require a fluorescence tracer. This attribute makes it possible to study a binary mixture, which simplifies modeling significantly.

Fluoroketone is also a reasonable surrogate because it has similar properties to the light ends of hydrocarbon fuels (many of the light ends are more likely to transition) and some alternative fuels. Novec has viscosity and vapor pressure that fall in the same range as the hydrocarbons, while its surface tension is a little bit lower than hydrocarbons (see Fig. 3).

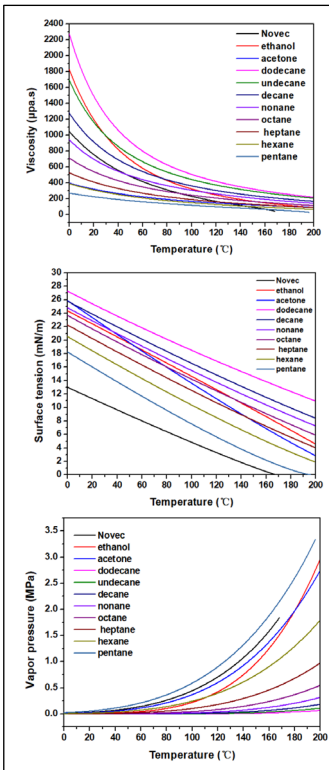

Figure 3. Novec properties using the NIST database.

For pure Novec (the fluid is in pure form inside the delivery system up to the nozzle exit), the critical pressure is P_c = 18.8 *bar*, and the critical temperature is T_c = 169 ˚*C*. The boiling point for pure Novec at 1 *bar* is T_{bp} = 49 ˚*C*. In the last few *cm* of the liquid delivery system we heat the fluid well above that temperature, but it is delivered at 15, 18, or 30 *bar* (depending on the experimental test case), and we detect no evidence for boiling inside the delivery system. All the same, the liquid can evaporate within the chamber. Evaporation is a common, interfering issue for transcritical fluid experimentation.

In order to develop experimental conditions for this study, it was necessary to understand vapor liquid equilibria (VLE) for fluoroketone/nitrogen mixtures in the chamber, which then identify the critical points for various mixture fractions (the critical locus). There are numerous equations of state (EoS) available for predicting the vapor-liquid coexistence region of binary mixtures. Two such EoS include the Peng-Robinson and PC-SAFT models. Linnemann and Vrabec[3] used a view cell to detect the critical points for Novec/N_2 mixtures by observing the disappearance of the liquid/gas interface at specific pressures and temperatures, for various mixture fractions. They then compared the performance of the Peng-Robinson and PC-SAFT models for the mixtures they had observed, and they reported that the PC-SAFT model matched the experimental data more closely. They provided model parameters for both components of the mixture.

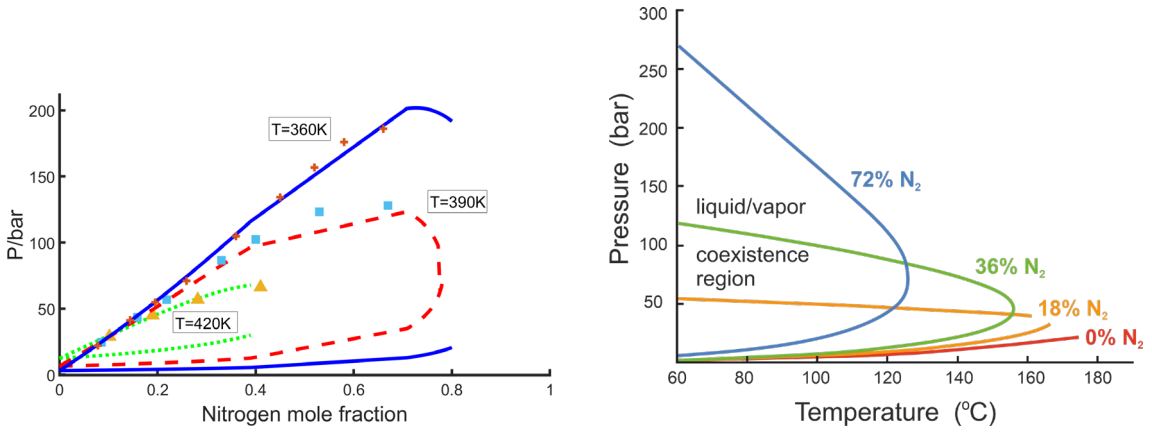

a. b.

Figure 4. a. Pressure vs N_2 mole fraction for Novec/N_2 mixtures at three temperatures. The data points are from Linnemann and Vrabec[3] and the curves were generated by FluidProp; b. Critical locus for Novec/N_2 mixtures predicted by FluidProp.

To establish conditions where vapor and liquid cannot co-exist within the chamber, it is useful to identify the critical locus on a graph of pressure against temperature. Here the commercial software FluidProp™ was used. In communication with the software developer, the model parameters were matched to the ones provided by Linnemann and Vrabec. The contours generated by this approach agreed with their experimental data, validating the model (see Fig. 4a). Subsequently, FluidProp was used to generate the P-T diagram depicted in Figure 4b. The results indicate a rapid increase in the critical pressure as nitrogen is added, whereas the critical temperature gradually decreases. The results in Figure 4 indicate that all mixtures of interest would fall outside the coexistence region (be supercritical once equilibrium has been established) if we hold temperature at or above 175 $^{\circ}C$. Note that for a mixture with 72% N_2, the critical pressure is around 265 *bar*, a pressure we cannot reach. The mixtures we have studied at $T_{chamber} > 175^{\circ}C$ would therefore be classified as "gas-like supercritical".

Six experimental test cases were developed (see Table 1), based upon these VLE estimates and some initial experiments using shadowgraphy to verify anticipated changes in the flow.

Table 1: Test cases

Test Case	T_{Novec} (^oC)	$T_{Chamber}$ (^oC)	$P_{chamber}$ (*bar*)§	Description
1	160	150	15	Subcritical jet into subcritical chamber
2	190	150	15	Superheated vapor ($T > Tc$ but $P < Pc$ inside injector) into subcritical ($T_{chamber} < 170\ ^{\circ}C$) chamber
3	170	170	18	Critical point (Tc & Pc inside injector) into critical point ($T_{chamber} = 170\ ^{\circ}C$) chamber
4	160	220	15	Subcritical (inside injector) into supercritical ($T_{chamber} > 175\ ^{\circ}C$) chamber
5	160	220	30	Compressed liquid ($P > Pc$ but $T < Tc$ inside injector) into supercritical ($T_{chamber} > 175\ ^{\circ}C$) chamber
6	190	220	30	Supercritical ($P > Pc$ and $T > Tc$, inside injector) into supercritical ($T_{chamber} > 175\ ^{\circ}C$) chamber

§ Pressures are gage pressure.

Planar laser-induced fluorescence (PLIF) and planar elastic light scattering (PELS):

DeSouza and Segall[4] have explored the photo-physics of fluoroketone in detail. It can absorb laser radiation at the third harmonic of Nd:YAG (355 *nm*), but that wavelength is near the edge of the absorption spectrum. The fluorescence spectrum peaks near 420 *nm*. The absorption and emissions spectra touch in the wings but do not strongly overlap, so radiative trapping of the fluorescence is not a major issue.

In this work, the output of a Quantel pulsed Nd:YAG laser in the third harmonic was spread into a sheet using three cylinder lenses (see Fig. 5). The sheet vertical dimension (~ 40 *mm*) was set by a 50 *mm* focal length cylinder lens followed by a 500 *mm* focal length cylinder lens (both lenses with their cylinder axes oriented horizontally). The ~ 2.5 *mm* thick sheet (illuminating the entire jet) was established by a third 750 *mm* focal length cylinder lens (with its cylinder axis oriented vertically). We rely upon linear fluorescence (at 60 *mJ* per pulse, linearity was confirmed by measurement) because we did not detect problems with optical depth in our initial work, and linear fluorescence makes scaling easier. In the images, we assume the fluid exiting just at the nozzle is 100% Novec (and here the density is estimated using FluidProp), while 0% is the background level acquired during every experiment. We also assume that fluorescence is linear in number density. The 100 PLIF images per test case and location were background subtracted and corrected for the laser sheet profile, which was acquired by imaging the sheet using surface scattering from a uniform card.

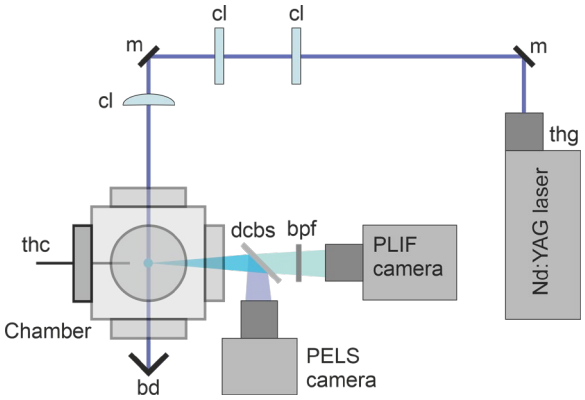

Figure 5. Optical layout: thg = third harmonic generator, m = mirror, cl = cylinder lens, thc = thermocouple, bd = beam dump, dcbs = dichroic beam splitter, bpf = bandpass filter.

The sheet of laser light at 355 *nm* will also scatter elastically from an intact liquid interface (called planar elastic light scattering, PELS, here). This signal can be used to detect when the interface is strong, when it is weakening, and when it has disappeared. Loss of interface scattering could be caused by a supercritical transition or because the liquid has vaporized entirely; this measurement alone is not sufficient to decide whether the fluid has gone supercritical, but it is a contributing piece of information.

Because the subcritical jets are not optically thick, the laser sheet enters and is reflected around inside the liquid before exiting towards the camera. The camera collects image signatures of randomly varying caustics for that reason. All the same, caustics are evidence for interface scattering. Because the jet undergoes Rayleigh breakup when surface tension is present, small wave structures are developed across the interface and these structures locate the strongest caustics. Even under subcritical conditions, however, the Novec is vaporizing so the liquid column will shrink over time.

To analyze these data, we acquire 200 PELS images, subtract the background from each, normalize each of them for the laser sheet profile, and then average all 200 images. We then average each radial signature at each axial position to give an averaged scattering signal as a function of axial distance.

Two PLIF campaigns were conducted. In the first campaign, all six test cases were imaged on-axis and off-axis, imaging as much of the overall jet as possible. PLIF was used in combination with PELS, as shown in Fig. 5. Following that work, we selected the most interesting cases and performed magnified PLIF imaging on-axis, in order to acquire higher resolution images of the mixture fraction. PELS was not included in that campaign so that we could eliminate the dichroic beam splitter and position the camera closer to the flow.

In the first PLIF campaign, as shown in Fig. 5, the PLIF/PELS imaging system used a 2 inch dichroic beam splitter in front of the exit window, reflecting 355 *nm* light to an Andor iXon Ultra EMCCD camera (used for PELS) and passing fluorescent light to a Princeton Instruments Pi-MAX4 1024i camera (for PLIF) equipped with a bandpass filter centered at 420 *nm* and a bandwidth of 10 *nm* FWHM. The Andor camera was fitted with a 50 *mm* focal length lens (providing spatial resolution of 54 μm/pixel) while the Pi-MAX was fitted with a 105 *mm* focal length lens (providing spatial resolution of 45 μm/pixel, although that figure ignores image smearing caused by the intensifier). The camera images were registered to each other, but since the imaging chips have different dimensions the exercise only ensured that we viewed the same field at the same magnification. Distances were calibrated for both cameras by imaging a high resolution ruler located in the image plane. PLIF/PELS images presented here were taken on the jet centerline.

In the second PLIF campaign, the dichroic beam splitter was removed but the bandpass filter was retained. The Andor iXon Ultra EMCCD camera was used for magnified PLIF because it can achieve better spatial resolution than the PiMAX. A 105 mm lens was used with a 50 *mm* lens extender to give a spatial resolution of 17 μm/pixel. Test cases 2, 3, 4 and 6 were studied here, as the others were considered sufficiently well understood after the first PLIF campaign.

The PLIF results for the second campaign contained some evidence for absorption of the laser sheet across the liquid column. This issue was not obvious in the first campaign results, probably because the column was a smaller part of each image and the camera used did not have the same spatial resolution. Therefore, the *averaged* PLIF images for campaign two were adjusted for Beer's law absorption across the core, but the left hand side of the images (especially the single images, which have no correction) is more reliable as that side needed no correction.

Temperatures The chamber is highly repeatable and steady. For this reason we decided to use simple thermocouples to measure temperatures. To monitor the thermocouple location we used two cameras. An end-on camera was used to ensure that the thermocouple bead was on the jet centerline. A second camera viewed the system at 90 degrees to the first camera, and it was used to locate the bead in the plane.

Results and Discussion

PELS results:

The PELS images were analyzed as described above. Figure 6 includes the results for the six test cases provided in Table 1. The images were corrupted by scattering from the nozzle within the first few *mm*, so the PELS data start at 2.5 *mm* below the nozzle outlet. In Figure 6, one can see that there is a significant scattering signal for cases 1, 4 and 5. These three cases use the same temperature for the injected liquid, and it is below T_c for the pure liquid. Those jet results include evidence for interfacial scattering. The oscillations in cases 1 and 5 are repeatable; they are established by the wave structure in the liquid column. Case 4 did not have strong wave structure or oscillations. The difference between cases 4 and 5 is that case 5 was at twice the pressure. The test case 1 curve has two slopes, with a steeper slope between 2.5 and 12.5 *mm* axial distance, and a reduced slope afterwards. This happens because the average intact liquid length for that jet is 12.5 *mm*. Past that point, gaps between drops reduce the slope of the averaged curve. Note that the curve for test case 5 does not have the same change of slope, and the magnitude between 2.5 and 12.5 *mm* axial distance is fairly low compared to case 1, implying a weakening of the interface.

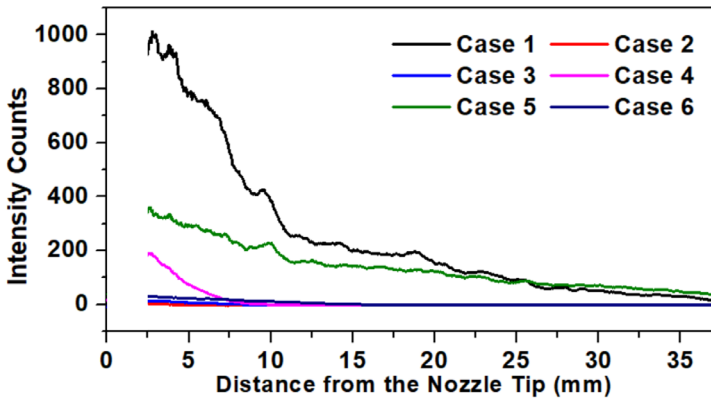

Figure 6. PELS results for the jets under the test cases listed in Table 1. The average standard deviations in the data were: σ_1 = 143, σ_2 = 1.1, σ_3 = 1.4, σ_4 = 16, σ_5 = 25, and σ_6 = 2.2.

The other cases shown use a temperature inside the injection system that is at or above T_c for the pure liquid. Those test cases exhibit no evidence of elastic scattering.

First PLIF campaign results:

Combined PLIF and PELS images for each test case are presented here. The PLIF images include one characteristic single image together with an average of 100 images. The corresponding elastic scattering data are included for reference.

Figure 7a. (test case 1), for the subcritical case, shows a jet undergoing Rayleigh breakup, albeit at a high chamber temperature (modifying the liquid physical properties at the interface). The liquid length mentioned above is obvious.

Figure 7b. (test case 2) is for a superheated vapor ($T > T_c$ but $P < P_c$) inside the nozzle. The chamber temperature was below T_c for the mixture. Here the images indicate a moderately dense gas jet at the nozzle outlet; the jet is diffuse and sinuous, and there is no interface scattering signal. The jet probably entered the chamber as a vaporizing fluid. The chamber is subcritical but above the boiling point, so it is likely that a subcritical vapor would be found around and below the jet.

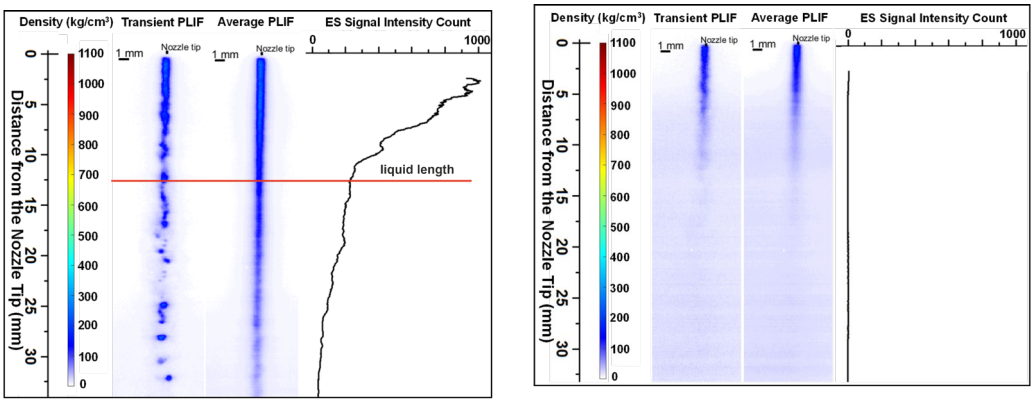

a. b.

Figure 7. Combined PLIF and PELS for: a. Test case 1; T_{Novec} = 160 ° *C*, $T_{chamber}$ = 150 ° *C*, and $P_{chamber}$ = 15 *bar* (gage), and b. Test case 2; T_{Novec} = 190 ° *C*, $T_{chamber}$ = 150 ° *C*, and $P_{chamber}$ = 15 *bar* (gage).

Test case 3 (Figure 8a.) is very close to the critical point for the pure liquid inside the nozzle and for the chamber. Holding the liquid near the critical point inside the fluid delivery system can produce an instability, although the test case 3 in Table 1 is stable and reproducible. When operating in the other five test cases in Table 1, we found that the liquid control thermocouple was usually less than 10 °*C* lower than the liquid outlet temperature (there is heater tape wound around the tube in between the control thermocouple and nozzle outlet, so the exit temperature is always higher than the control temperature). For case 3, however, the difference can easily reach 30 °*C* and it can become difficult to stabilize the temperature. This behavior is consistent with the findings of Fu and Lin[5], who show the pure Novec thermal conductivity shoots up at the critical point and then falls back down. This image depicts a dense but diffuse, sinuous jet and there is no evidence for elastic scattering.

Test case 4 (Figure 8b.) is for a subcritical pure liquid issuing into a chamber that is supercritical (based upon our VLE estimates). Within the first 10 *mm* the PLIF image shows some very weak wave structure on the jet surface and there is an elastic scattering signal. Beyond that axial location the elastic scattering signal has disappeared and the jet has become diffuse and sinuous before disappearing. It is unclear whether or not the downstream mixture became supercritical.

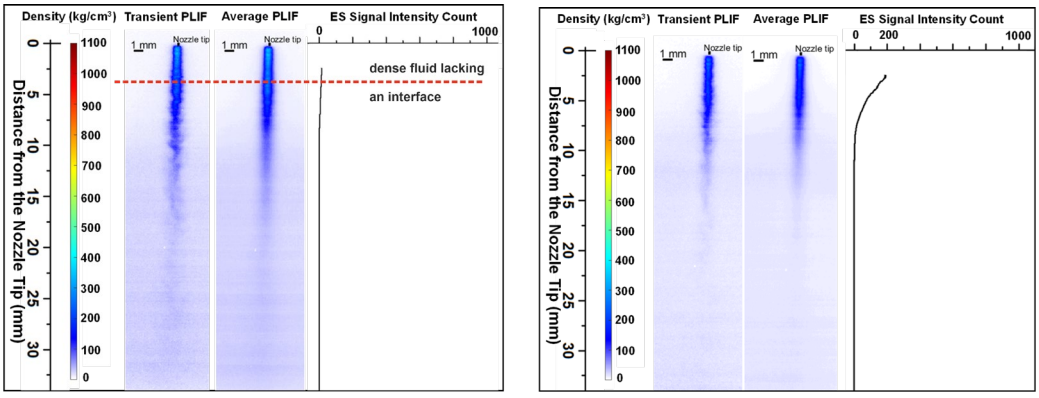

a. b.

Figure 8. Combined PLIF and PELS for: a. Test case 3: T_{Novec} = 170 ° *C*, $T_{chamber}$ = 170 ° *C*, and $P_{chamber}$ = 18 *bar* (gage), and b. Test case 4: T_{Novec} = 160 ° *C*, $T_{chamber}$ = 220 ° *C*, and $P_{chamber}$ = 15 *bar* (gage).

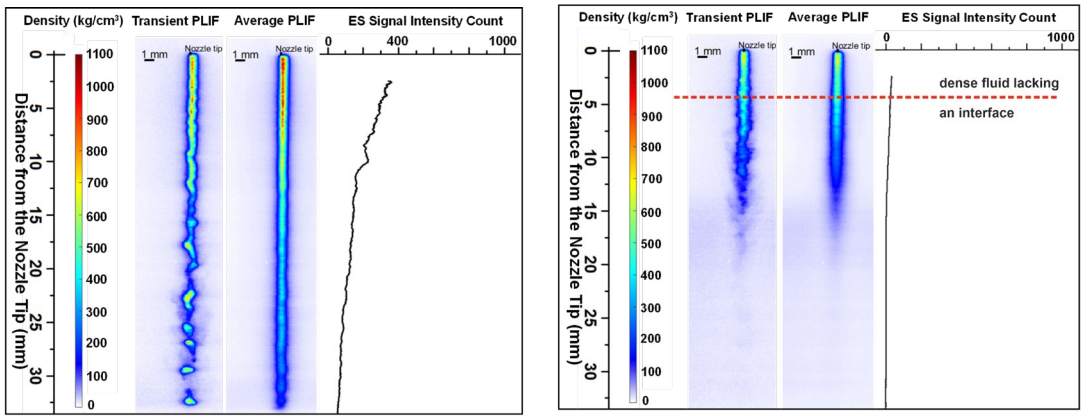

a. b.

Figure 9. Combined PLIF and PELS for: a. Test case 5: T_{Novec} = 160 ° *C*, $T_{chamber}$ = 220 ° *C*, and $P_{chamber}$ = 30 *bar* (gage), and b. Test case 6: T_{Novec} = 190 ° *C*, $T_{chamber}$ = 220 ° *C*, and $P_{chamber}$ = 30 *bar* (gage).

Figure 9a. contains data for test case 5. Here the pure Novec was a compressed liquid inside the nozzle (*T* < *Tc* but *P* > *Pc*). The chamber was supercritical according to our VLE estimates. The LIF signal was stronger because the density was higher. This jet was neither supercritical nor was it fully vaporized, because there was clear evidence for surface scattering and the jet was undergoing Rayleigh breakup (with a liquid length of 12.5 *mm* again). The PELS signal is significantly lower than it was for case 1, however. The only difference between Figures 8b. and 9a. is that the data in Figure 9a. are for a pressure that is twice the pressure of Figure 8b. Here, the Novec boiling point increased with pressure, significantly reducing the rate of vaporization.

Finally, test case 6 results are shown in Figure 9b. Here the pure Novec inside the nozzle was supercritical, while the chamber was also supercritical according to our VLE estimates. The PLIF images imply a jet similar to that of case 5 within the first few *mm*, but one that disappears quickly. The scattering data, however, indicate that there was no well-defined liquid/gas interface.

As already mentioned, the disappearance of an interface can be caused either by transition to a supercritical state or by evaporation. The chamber was hot enough to support evaporation, as evidenced by the falling curves for test cases 1, 4 and 5. As liquid elements evaporate, however, the vapor mixes across the chamber and the PLIF image of the remaining liquid weakens substantially. The vapor becomes a uniform background across the entire chamber (the entire chamber was not imaged here). Some of our test cases do not exhibit those trends and they might contain supercritical regions.

There are regions where the PLIF image indicates a fluid density on the same order as the subcritical density, but there is no evidence for interface scattering. Examples include the regions marked with a red dashed line in Figures 8a. and 9b. There is a reasonable chance that those datasets indicate a supercritical jet. Case 6 (Figure 9b.) holds all conditions above the critical point, and if any of our jets were supercritical it would be this one. Those PLIF images indicate a sinuous, dense gas jet. Case 3 could potentially have supercritical locations as well. The lower parts of test case 4 may also be supercritical.

Second PLIF campaign results:

Here one camera was used for magnified PLIF as described above. There are no PELS data for this campaign but we assume the scattering information has not changed. In this campaign the goal was to image Novec density distributions at higher spatial resolution. Typical results for test cases 2, 3, 4 and 6 are included. In addition to the images, we present plots of Novec density vs. radius at four axial positions for those same four test cases. These radial plots were generated using averaged images, so there is some smearing of profiles generated by small variations from image to image. All the same, averages provide a more robust comparison to averaged CFD results.

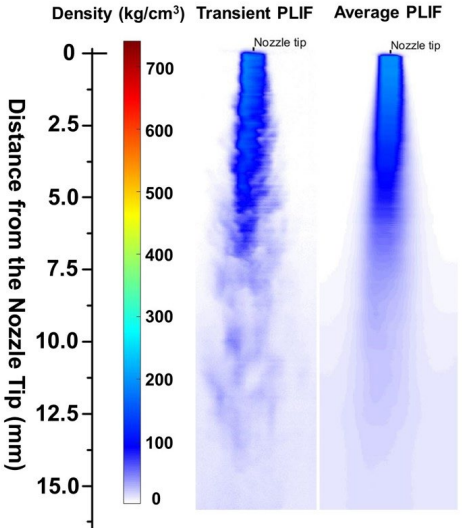

a.

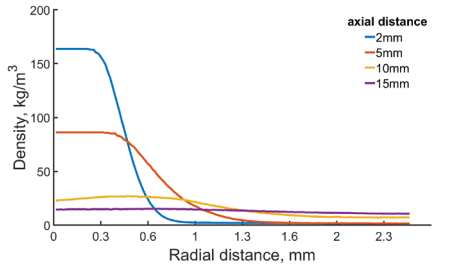

b.

Figure 10. a. Test case 2, magnified PLIF, b. Novec density vs. radius & axial distance.

Figure 10 contains results for test case 2 (a superheated vapor ($T > T_c$ but $P < P_c$) inside the nozzle). The chamber temperature was below T_c for the mixture. As before, the images indicate a moderately dense gas jet at the nozzle outlet. There was no interface scattering signal. It is likely that a subcritical vapor would be found around and below the jet. The density plots (taken from the average image) are not surprising, spreading out with axial distance.

Test case 3 (Fig. 11) is very close to the critical point for the pure liquid inside the nozzle and for the chamber. The density is higher in this case because the pressure was increased from case 2 while the temperature was somewhat lower. The density plots indicate a concommitant increase of density in the core, even with distance, but gradients along the edge are similar.

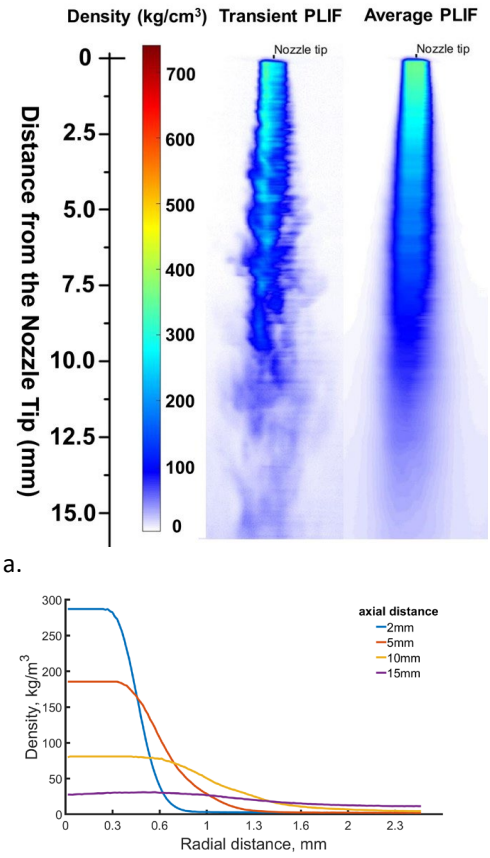

a.

Figure 11. a. Test case 3, magnified PLIF, b. Novec density vs. radius & axial distance.

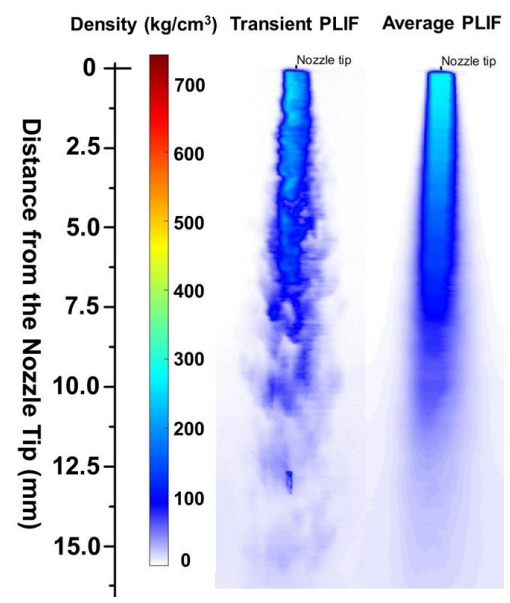

a.

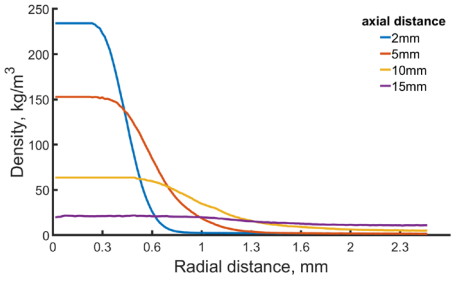

b.

Figure 12. a. Test case 4, magnified PLIF, b. Novec density vs. radius & axial distance.

Test case 4 (Figure 12) is for a subcritical pure liquid issuing into a chamber that is supercritical (based upon our VLE estimates). The density is a bit lower than test case 3 mostly because the pressure was reduced again. In this case there was an elastic scattering signal within the first 10 *mm*, but beyond that point the elastic scattering signal disappeared. The average density gradients are similar to the others.

Test case 6 results are shown in Figure 13. Here the pure Novec inside the nozzle was supercritical, while the chamber was also supercritical according to our VLE estimates. The density is high because the pressure was double the pressure used in cases 2 and 4. Otherwise the density distributions are similar. These data support the conclusions in the section above where it is argued that the density distributions for cases 3 and 6 are similar to subcritical jets but they have no evidence for surface scattering. Those are likely supercritical cases.

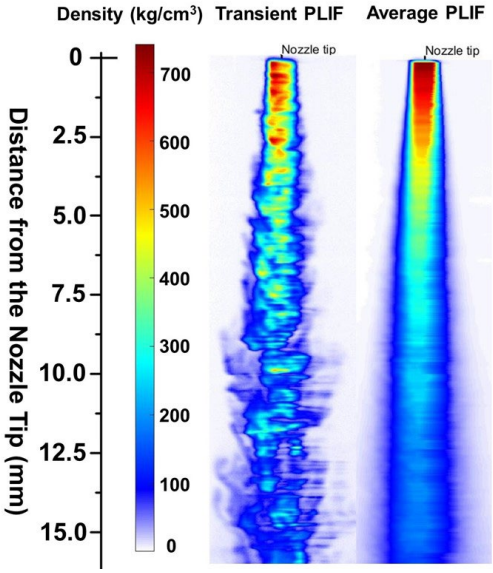

a.

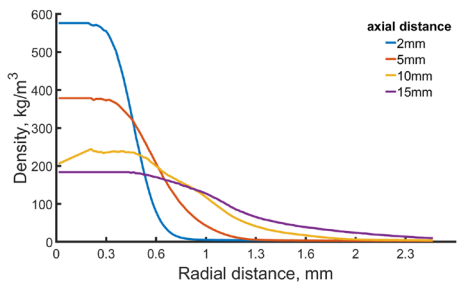

Figure 13. a. Test case 6, magnified PLIF, b. Novec density vs. radius & axial distance.

Temperature profiles:

Temperature maps for cases 2, 3, 4 and 6 are shown in Figure 14. Here the discrete locations of the thermocouple are marked by dots. The measured temperatures were interpolated across the 2-D plane to produce these images. Interestingly, in case 6 the temperature falls on centerline, and the temperature decrease is outside the measurement uncertainty. We have given this phenomenon serious consideration and consulted with our collaborators about this issue. It should not happen because the chamber is even hotter than the injectant, and there is supposed to be no phase change under these conditions (no evaporative cooling). For now we have no explanation for this phenomenon.

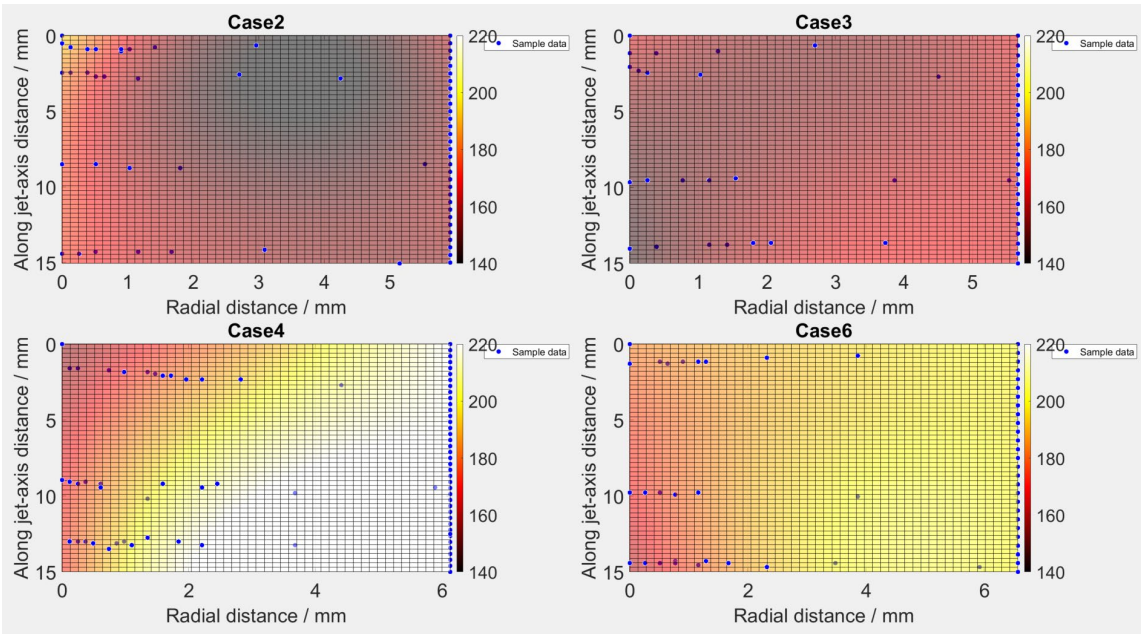

Figure 14. Temperature maps for the four test cases studied in the second PLIF campaign.

Conclusions and future work

We have generated a more comprehensive dataset than prior work. It is for a simple, pure liquid jet issuing into a pure gas under various thermodynamic conditions. The data include information on the strength of the liquid/gas interface, mixture as a function of position, and local temperature. These results could be used by modelers who would be willing to incorporate this fluoroketone into their codes.

At the time of this writing, we are setting up a four-wave mixing technique called laser induced thermal acoustics (LITA). Sound speed reaches a minimum at the supercritical state, so LITA will be used to measure the local sound speed at a single point (with the sample volume scanned across the jet to detect spatial and temporal variations). We will focus on locations of interest in test cases 2, 3, 4 and 6.

Laser Induced Thermal Acoustics (LITA) - Ewart and co-workers developed a high-precision combustion temperature measurement called laser induced thermal grating spectroscopy (LITGS), inferring temperature from a measured sound speed[6]. In this work, we have collaborated with the Ewart group to develop and apply a closely related technique called laser induced thermal acoustics (LITA), aimed at directly measuring the sound speed at a single point. The technique relies upon generation of an index grating in a flow-field, by splitting a pulsed laser beam into two beams and crossing them to produce a small sample volume. Figure 15 contains a schematic representation of two laser beams crossing each other at angle θ. They interfere to produce the vertical grating shown, with grating wavelength $\Lambda = \frac{\lambda}{2\,sin(\theta/2)}$, where λ is the wavelength of the laser light. If the laser is tuned to a molecular resonance (355 nm for fluoroketone), the grating pattern is absorbed during the pulse, producing a spatial modulation of excited state populations (i.e. a population grating). After the pulse has passed, the population grating quickly thermalizes to produce a thermal grating. Both a stationary thermal grating and a standing-wave acoustic grating produced by collisions with neighboring molecules (forming two counter-propagating acoustic waves) can be set up. These gratings induce a spatially and temporally varying index of refraction in the gas. A third, continuous-wave probe beam is then Bragg-scattered off of the index grating to generate a signal beam. The scattered beam is imbedded with a time dependence that oscillates and decays at rates that are dependent upon the local thermodynamic and transport properties of the gas mixture (see Figure 16 which contains acetone data from our lab). If one measures the temporal period of acoustic oscillation (τ_{osc}) one can infer the sound speed $c = \Lambda / \tau_{osc}$, if Λ has been found by one of several means. The trace actually provides the sound speed directly; no special modelling is required. LITA will be applied to the jet experiment to detect sound speed and thermal grating diffusion rate within the sample volume defined by the beam crossings, at various locations relative to the jet.

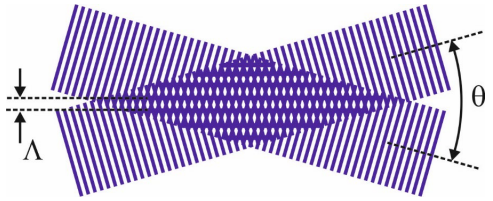

Figure 15. Beam overlap generating an interference, and when absorbed the Λ fringe becomes a population grating.

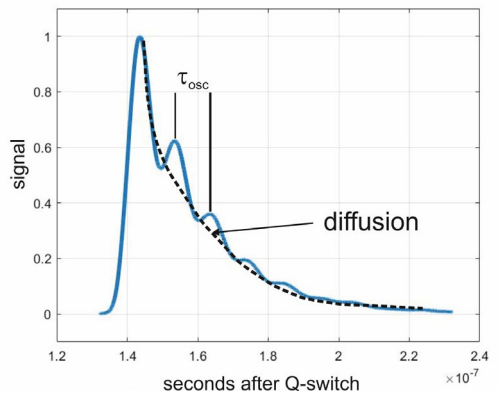

Figure 16. Experimental LITA signal in acetone.

Publications

- "Improving the spatial dynamic range of digital inline particle holography", Zachary Falgout, Yi Chen, and Daniel R. Guildenbecher, Applied Optics, Vol. 58, Issue 5, pp. A65-A73 (2019), doi.org/10.1364/AO.58.000A65
- "Optical Diagnostics for High Pressure Sprays", chapter in the book *High Pressure Flows for Propulsion Applications*, edited by Josette Bellan, Jet Propulsion Laboratory, California Institute of Technology, Published by American Institute of Aeronautics and Astronautics, ISBN 978-1-62410-580-7, (2019).
- "Optical spray imaging diagnostics", chapter in the book *Optical Combustion Diagnostics for Propulsion and Power Systems: Theory and Application*, edited by Adam Steinberg, Georgia Tech, and Sukesh Roy, Spectral Energies Inc., to be published by American Institute of Aeronautics and Astronautics, (anticipated 2022).
- "Laser imaging of sub-/trans-/ and super-critical interfaces", Georgios Kasapis, Shangze Yang, Zachary Falgout and Mark Linne, under review for publication in the Proceedings of the Combustion Institute and presentation at the 39th International Symposium on Combustion, Vancouver, Canada 24 – 29 July, 2022. The first round of reviews raised no serious problems.
- "Detailed investigation of sub-/trans-/ and super-critical interfaces", Georgios Kasapis, Shangze Yang, Zachary Falgout and Mark Linne, in preparation for submission to Physics of Fluids.
- A paper presenting the LITA results in Novec will be prepared when the experiments have been completed.
- "Detailed investigation of sub-/trans-/ and super-critical interfaces", Georgios Kasapis, PhD thesis, in preparation.

References

[1] Z. Falgout, M. Rahm, D. Sedarsky, and M. Linne, Fuel, **168**, 14-21, (2016).
[2] K. Harstad, J. Bellan, Combustion and Flame, 127, 1861–1879 , (2001).
[3] M. Linnemann, J. Vrabec, Journal of Chemical and Engineering Data 62 (7) (2017) 2110–2114.
[4] S. DeSouza, C. Segal, in: J. Bellan (Ed.), High Pressure Flows for Propulsion Applications, American Institute for Aero- nautics and Astronautics Inc., Reston, VA, 2020.
[5] B.-R. Fu, W.-J. Lin, International Communications in Heat and Mass Transfer 117 (2020) 104740.
[6] P. Ewart and S.V. O'Leary, Optics Letters, 11(5), pp. 279-281, (1986); H. Latzel, A. Dreizler, T. Dreier, J. Heinze, M. Dillmann, W. Stricker, G. M. Lloyd, P. Ewart, Applied Physics B **67**, 667, (1998).